




Thickness-tunable magnetic and electronic transport properties of the quasi-two-dimensional van der Waals ferromagnet $\text{Co}_{0.27}\text{TaS}_2$ with disordered intercalation

Hanin Algaidi ¹, Chenhui Zhang,¹ Chen Liu,¹ Dongxing Zheng,¹ Yinchang Ma ¹, Youyou Yuan,² and Xixiang Zhang ^{1,*}

¹Physical Science and Engineering Division (PSE), King Abdullah University of Science and Technology (KAUST), Thuwal 23955-6900, Saudi Arabia

²Core Labs, King Abdullah University of Science and Technology (KAUST), Thuwal 23955-6900, Saudi Arabia



(Received 7 January 2023; accepted 27 March 2023; published 6 April 2023)

The intercalation of magnetic elements in nonmagnetic van der Waals (vdW) materials is an effective way to design different (quasi) 2D magnets and produce exotic properties. More specifically, how exactly the intercalator is distributed within the synthetic crystal can also affect the physical properties substantially. In contrast to conventional 3d transition-metal intercalates of niobium and tantalum dichalcogenides, which commonly have 2×2 or $\sqrt{3} \times \sqrt{3}$ type ordered intercalation, we report a disordered intercalation of Co atoms between the vdW gaps of 2H-tantalum disulfide (2H-TaS₂). The obtained quasi-vdW ferromagnet $\text{Co}_{0.27}\text{TaS}_2$ shows both perpendicular magnetic anisotropy and thickness-tunable magnetic properties. More interestingly, the temperature dependence of electrical resistivity shows a semiconductorlike behavior, in contrast to the metallic feature of other analogs in this material family. This unexpected phenomenon can be understood through a variable-range hopping mechanism, which is due to highly disordered intercalation. Moreover, $\text{Co}_{0.27}\text{TaS}_2$ shows a side-jump scattering dominated anomalous Hall effect, which can also be related to the disordered distribution of Co intercalators.

DOI: [10.1103/PhysRevB.107.134406](https://doi.org/10.1103/PhysRevB.107.134406)

I. INTRODUCTION

Since physical properties are affected as the dimensionality is reduced, van der Waals (vdW) materials have grabbed great interest for their weakly bonded layered structure that facilitates the exfoliation to reach a few layers or even monolayers [1–5]. In 2017, exfoliated CrI_3 and $\text{Cr}_2\text{Ge}_2\text{Te}_6$ flakes, as thin as one or two layers, were shown to retain their intrinsic magnetic properties. This showed the potential of vdW materials for studying the magnetic properties in true two-dimensional (2D) limits and for applications in spin-based devices [6–9]. To expand the 2D magnetic material family, one effective method is to intercalate magnetic ions or magnetic molecules into the vdW gap (between the weakly bonded layers). The introduction of these intercalators can modulate the crystal structure and interlayer coupling significantly and allow tuning of the magnetic and electronic properties [10]. 3d transition-metal intercalates of niobium and tantalum dichalcogenides have the empirical formula of T_xMD_2 ($T = \text{V, Cr, Mn, Fe, Co, Ni}$; $M = \text{Ta, Nb}$; $D = \text{S, Se}$; $x = 1/4, 1/3$) exhibit either ferromagnetic or antiferromagnetic order, depending on their chemical composition and crystal symmetry

[11–14]. For instance, Fe_xTaS_2 shows ferromagnetic order with a magnetic easy axis that is aligned with the c axis for x ranging 0.2–0.4. However, the material becomes antiferromagnetic when x exceeds 0.4 [11,15,16]. Importantly, such synthetic T_xMD_2 can maintain the magnetic order even at atomic thickness [17,18], which makes it a promising candidate for low-dimensional spintronic applications.

According to previous studies, in the T_xMD_2 material family, intercalation always results in 2×2 or $\sqrt{3} \times \sqrt{3}$ superstructures, which leads to either the centrosymmetric $P6_3/mmc$ or chiral $P6_322$ space group [11]. For instance, $\text{Mn}_{1/4}\text{NbS}_2$, in which the Mn atoms form 2×2 superstructures, is a normal ferromagnet with a Curie temperature (T_C) of about 104 K [19]. $\text{Mn}_{1/3}\text{NbS}_2$, on the other hand, becomes a chiral helimagnet because the $\sqrt{3} \times \sqrt{3}$ ordered Mn intercalators modify the positions of the S atoms slightly, which produces a chiral crystal structure as well as significant Dzyaloshinskii-Moriya interaction [20]. Therefore, the symmetry of intercalators represents an important degree of freedom that can alter the magnetic properties substantially. However, unlike the ordered 2×2 and $\sqrt{3} \times \sqrt{3}$ type intercalation, the disordered intercalation of magnetic atoms in T_xMD_2 has neither been observed nor discussed. It would also be important to learn how this type of disorder can affect the electric and magnetic properties of the host material.

In this work, we report the disordered intercalation of Co atoms in 2H-TaS₂. The intercalation is confirmed using single-crystal x-ray diffraction (SC-XRD) and electron diffraction experiments. Because of the disordered

*xixiang.zhang@kaust.edu.sa

Published by the American Physical Society under the terms of the [Creative Commons Attribution 4.0 International](https://creativecommons.org/licenses/by/4.0/) license. Further distribution of this work must maintain attribution to the author(s) and the published article's title, journal citation, and DOI. Open access publication funded by King Abdullah University of Science and Technology.

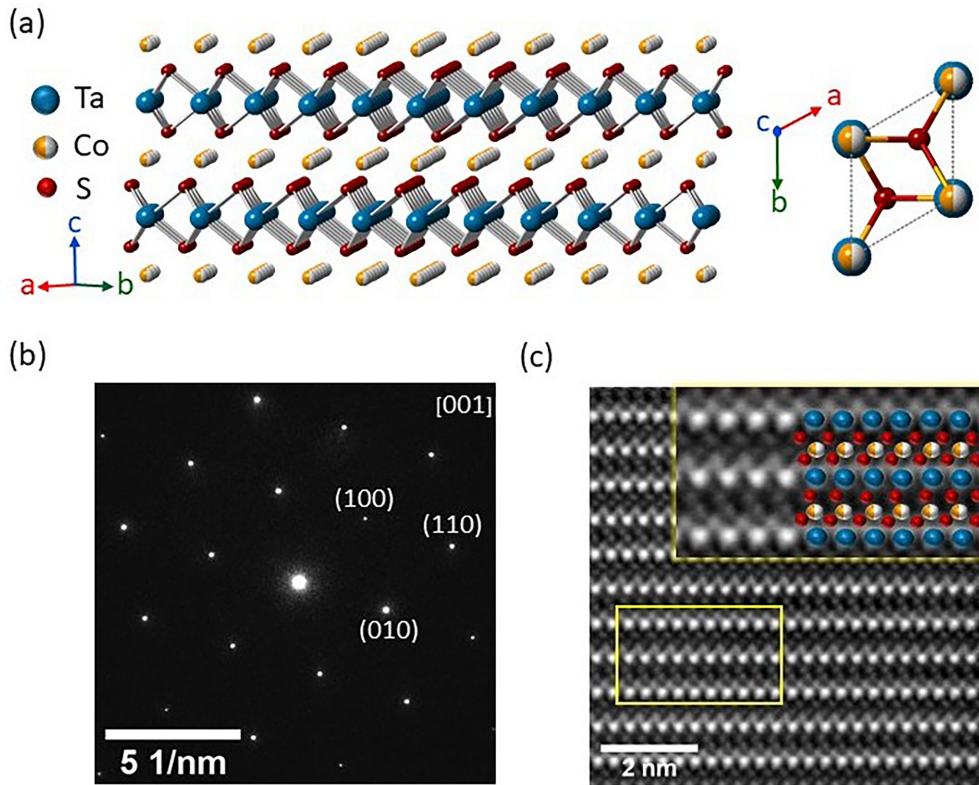


FIG. 1. (a) Schematic presentation of the $\text{Co}_{0.27}\text{TaS}_2$ structure. The unit cell of the crystal is marked by dashed lines. (b) SAED diffraction pattern of the $\text{Co}_{0.27}\text{TaS}_2$ crystal along the [001] direction. (c) Cross-section atomic-resolution STEM image of $\text{Co}_{0.27}\text{TaS}_2$ along the [010] zone axis. The inset shows the enlarged image to see the individual atoms more clearly.

intercalation, the temperature-dependent electrical resistivity of $\text{Co}_{0.27}\text{TaS}_2$ displays a semiconductorlike feature and can be described by the variable-range hopping mechanism. Moreover, $\text{Co}_{0.27}\text{TaS}_2$ can be exfoliated into thin flakes of different thicknesses, and their magnetotransport properties are studied. The anomalous Hall effect (AHE) mechanism in $\text{Co}_{0.27}\text{TaS}_2$ is mainly due to side-jump scattering, which can also be associated with disordered intercalation.

II. EXPERIMENT

A. Sample preparation and characterization

$\text{Co}_{0.27}\text{TaS}_2$ crystals were grown using chemical vapor transport (CVT) [21]. A stoichiometric mixture of Co, Ta, and S powder and a small amount of iodine was sealed in an evacuated quartz tube, which was placed into a horizontal two-zone furnace with a reaction-zone temperature of 1050°C and a growth-zone temperature of 900°C for seven days. The θ - 2θ XRD measurements were performed at room temperature using a Bruker D2 PHASER diffractometer with $\text{Cu } K_\alpha$ radiation ($\lambda = 1.54184 \text{ \AA}$). In addition, SC-XRD measurements were conducted using a Bruker D8 Venture diffractometer with $\text{Mo } K_\alpha$ radiation ($\lambda = 0.71073 \text{ \AA}$) at 180 K. The crystal structure was refined using the computer program SHELXT and the OLEX2 software package [22]. The scanning transmission electron microscopy (STEM) images were obtained using an FEI Titan Cs Probe transmission electron microscope.

B. Magnetic and transport measurements

The magnetic properties were investigated using a superconducting quantum interference device magnetometer (MPMS3, Quantum Design). The *h*-BN-covered devices were fabricated using the dry transfer method on an accurate transfer platform (Metatest, E1-M) with the assistance of polydimethylsiloxane (PDMS) stamps [23]. Hall bar devices were fabricated using electron beam lithography (EBL) after the mechanical exfoliation of a crystal. The electronic properties of both bulk and nanoflake devices were acquired using the four-probe method via a physical property measurement system (Quantum Design).

III. RESULTS

Figure 1(a) shows a schematic of $\text{Co}_{0.27}\text{TaS}_2$ based on the SC-XRD experiments. The refined SC-XRD data indicate a chemical composition of $\text{Co}_{0.27}\text{TaS}_2$, which belongs to the $P6_3/mmc$ space group with the lattice parameters $a = 3.30870(10) \text{ \AA}$ and $c = 11.8788(5) \text{ \AA}$. The Co atoms intercalate between the vdW gaps of $2H\text{-TaS}_2$, forming octahedral coordination with the S atoms. More detailed SC-XRD results can be found in Table S1 of the Supplemental Material [24]. In addition, we also performed the energy-dispersive x-ray spectroscopy (EDX) to further confirm the chemical composition. The EDX result in Fig. S1 of the Supplemental Material [24] indicates a chemical formula of $\text{Co}_{0.26}\text{TaS}_{1.84}$ (with respect to Ta) or $\text{Co}_{0.28}\text{Ta}_{1.09}\text{S}_2$ (with respect to S), which is very

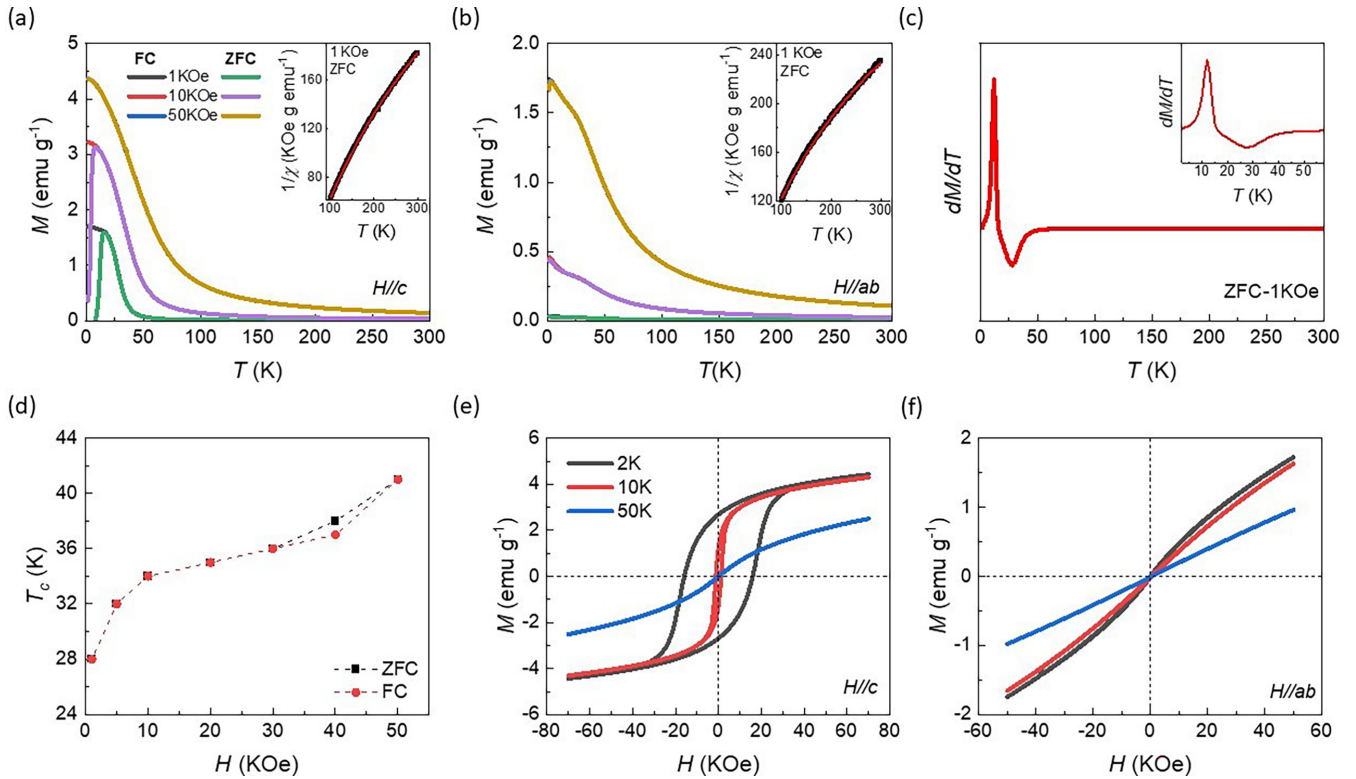


FIG. 2. Magnetic properties of bulk sample: (a),(b) Temperature-dependent magnetization along the c axis and ab plane, respectively. Inset: temperature dependence of the inverse susceptibility, with $H = 1$ kOe fitted by Curie-Weiss law. (c) Temperature-dependent dM/dT for the ZFC $M(T)$ curve. (d) The applied magnetic-field dependence of T_C . The dashed lines serve to guide the eye. (e),(f) The $M(H)$ curves were measured using $H//c$ and $H//ab$ at different temperatures. At 2 K and $H//c$, the coercive field H_c is 1.6 kOe.

close to the SC-XRD result. In Fig. S2, the $(00l)$ reflection peaks of the θ - 2θ XRD pattern reveal that the crystal surface is the ab plane. The selected area electron diffraction (SAED) pattern of $\text{Co}_{0.27}\text{TaS}_2$ along the $[001]$ direction, Fig. 1(b), shows hexagonally arranged diffraction spots with no additional superstructure spots. In the $T_x\text{MD}_2$ material family, the magnetic intercalators tend to form 2×2 or $\sqrt{3} \times \sqrt{3}$ ordered superstructures, which can be identified by the $(1/2 \ 1/2 \ 0)$ or $(1/3 \ 1/3 \ 0)$ diffraction spots in the $[001]$ direction in SAED patterns, respectively [25]. It is worth mentioning that the arrangement of intercalators plays an important role in the physical properties of the material [11,25]. Furthermore, the absence of superstructure diffraction spots in $\text{Co}_{0.27}\text{TaS}_2$ means that the Co atoms do not form 2×2 or $\sqrt{3} \times \sqrt{3}$ ordered configurations. Instead, they randomly occupy the center of S octahedrons within the vdW gap, with an average occupancy of 0.27, based on the SC-XRD results. Figure 1(c) displays a STEM image, which was acquired along the $[010]$ zone axis. The structural model can be overlaid perfectly with the STEM image, which confirms the validity of the determined crystal structure.

To obtain information about the magnetic properties of the materials, we first performed a temperature-dependent magnetization measurement with magnetic fields of 1, 10, and 50 kOe (applied along the c axis and ab plane), using both zero-field-cooled (ZFC) and field-cooled (FC) protocols for the bulk crystal. In Figs. 2(a) and 2(b), it is evident that the magnetization for $H//c$ is much higher than that for $H//ab$, which suggests perpendicular magnetic anisotropy (PMA).

The intrinsic T_C of the crystal can be obtained from the minimum of dM/dT using the low-field ZFC or FC curve. The extracted T_C for 1 kOe ZFC data was 28 K; see Fig. 2(c).

We also plotted the temperature dependence of $1/\chi$ (T) for the 1-kOe FC data in the inset of Figs. 2(a) and 2(b), for $H//c$ and $H//ab$. The data in the temperature range 100–300 K can be fitted well to the modified Curie-Weiss law, $\chi = \chi_0 + C/(T - \theta)$, where χ_0 is a temperature-independent term, C denotes the Curie-Weiss constant, and θ is the Weiss temperature. The parameters obtained for $H//c$ and $H//ab$, $\theta_c = 34.78$ K and $\theta_{ab} = -9.42$ K, indicate FM interactions along the c axis and AFM interactions along the ab plane, respectively. We also measured the ZFC-FC $M(T)$ curves for different magnetic fields to study if the T_C is field dependent because some magnetic 2D vdW materials exhibit a strongly field-dependent T_C . In Ref. [6], the magnetic-field dependence of T_C in a nano-thick $\text{Cr}_2\text{Ge}_2\text{Te}_6$ flake was reported but no such dependence was observed in the bulk limit. Figure 2(d) shows the extracted T_C as a function of the applied field along the c axis in the $M(T)$ measurements for the $\text{Co}_{0.27}\text{TaS}_2$ crystal. The T_C increased from 28 to 41 K when H increased from 1 to 50 kOe, and no sign of saturation could be observed. This suggests weak exchange coupling, which means that the applied field strength was comparable to the exchange field. As a result, T_C was enhanced by the external field. Note that the field dependence for fields below 10 kOe (and above 10 kOe) is also interesting and worthy of further investigation. To further validate the existence of PMA in the crystal, we performed the magnetization as a function of the applied

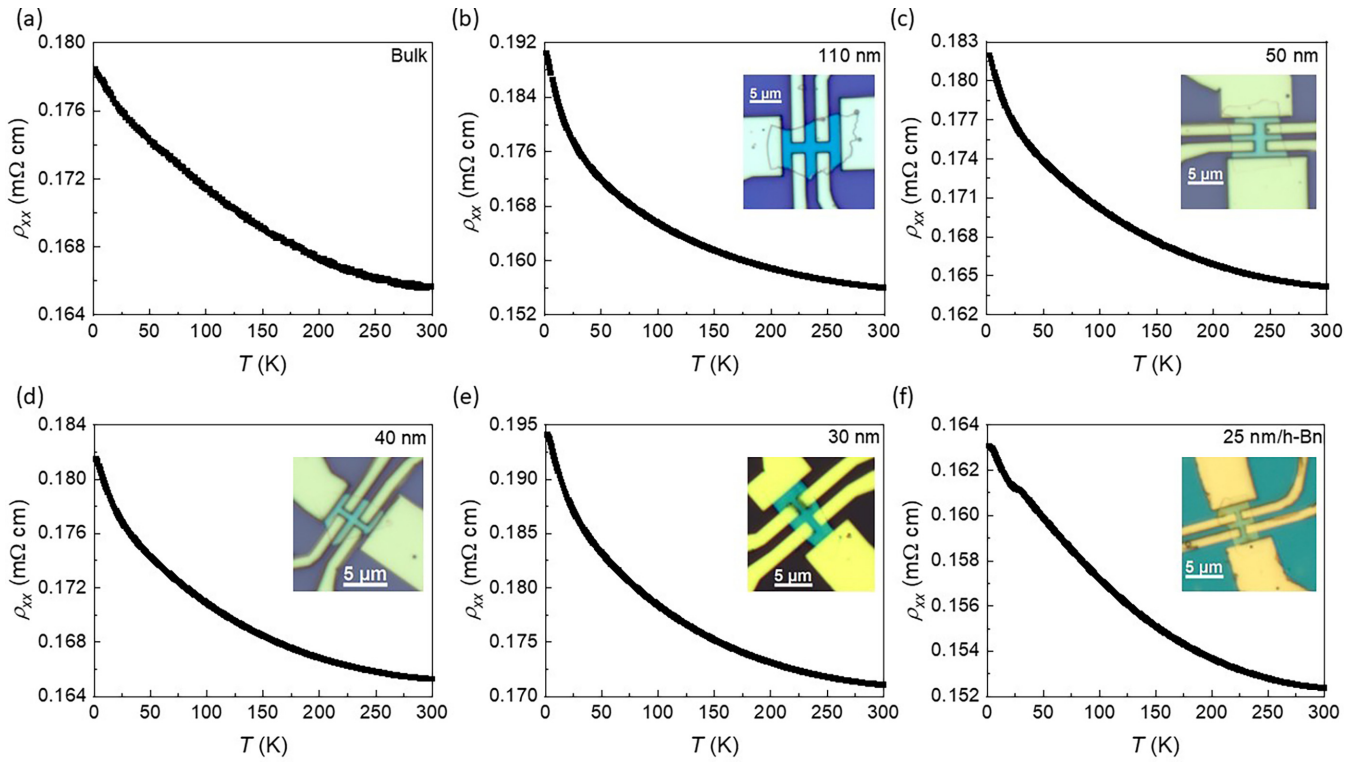


FIG. 3. Temperature dependence of the channel resistivity (ρ_{xx}) measured for bulk, 110-, 50-, 40-, 30-, and 25-nm devices. Inset: Optical image of the nano-thick-flake device.

magnetic field for both $H//c$ and $H//ab$ at different temperatures; see Figs. 2(e) and 2(f). When the field was applied along the c axis and the temperature was below T_C , hysteresis loops became clearly visible. The 2-K loops show a relatively high remanence, which confirms the presence of PMA (the magnetic easy axis is parallel to the c axis). The $M(H)$ curves for the $H//ab$ plane show no hysteresis loops, unsaturation, and reversible behavior across the whole temperature range, which further confirms the presence of PMA. At 50 kOe and 2 K, the magnetization for $H//c$ ($\sim 4 \text{ emu g}^{-1}$) is much higher than for $H//ab$ ($\sim 1.7 \text{ emu g}^{-1}$), which suggests the anisotropy field is much larger than 50 kOe. The nonperfect linear dependence of $M(H)$ for $H//ab$ below the Curie temperature and nonsquared hysteresis loops for $H//c$ indicate that the magnetic anisotropy is not perfectly perpendicular to the ab plane. A recent study showed that $\text{Co}_{1/3}\text{TaS}_2$, with Co atoms forming $\sqrt{3} \times \sqrt{3}$ superstructures, is a noncollinear antiferromagnet [26]. Even when the Co concentration decreases to 0.29 (i.e., $\text{Co}_{0.29}\text{TaS}_2$), the noncollinear antiferromagnetic order remains as long as the $\sqrt{3} \times \sqrt{3}$ superstructures persist [27]. Therefore, the clear differences in the magnetic properties between $\text{Co}_{0.27}\text{TaS}_2$ and $\text{Co}_{1/3}\text{TaS}_2$ (or $\text{Co}_{0.29}\text{TaS}_2$) should be on account of the different arrangements of the intercalators. Hence, a better understanding of the relationship between disordered intercalation and PMA in $\text{Co}_{0.27}\text{TaS}_2$ is needed.

To understand the charge transport mechanism in $\text{Co}_{0.27}\text{TaS}_2$, the magnetotransport properties, such as Hall resistivity and magnetoresistance, were measured for a temperature range 2–300 K and different thicknesses.

Figures 3(a)–3(e) show the temperature-dependent longitudinal resistivity ρ_{xx} for both the bulk and the nanoflakes with different thicknesses exfoliated from the same single crystal. The resistivity always increases monotonically with decreasing temperature across the whole temperature range, which suggests semiconductorlike behavior. However, the increase in resistivity is much weaker than in conventional semiconductors, since the ratio of $\rho(2 \text{ K})/\rho(300 \text{ K})$ is small (< 1.2). Thus, the temperature dependence of the electrical conduction in $\text{Co}_{0.27}\text{TaS}_2$ is expected to be dominated by barriers involved in the hopping/tunneling events instead of depending on the band gap of a typical semiconductor. In addition, both the resistivity value and the curve shape suggest that the charge transport is independent of the sample thickness down to 30 nm. To eliminate the probability of oxidization, which can cause such behavior, a device was fabricated for a flake, which was exfoliated in a glove box (argon atmosphere with $\text{O}_2 < 0.1 \text{ ppm}$ and $\text{H}_2\text{O} < 0.1 \text{ ppm}$) from a different crystal and then covered with h -BN. The longitudinal resistivity of the device, Fig. 3(f), confirms that the origin of the behavior stems not from the oxidization of the thin plates; instead, it appears to be intrinsic. This indicates that the semiconductorlike behavior is due to the disordered intercalation of Co atoms in $\text{Co}_{0.27}\text{TaS}_2$. Moreover, previous studies of $\text{Co}_{0.26}\text{TaS}_2$ and $\text{Co}_{0.29}\text{TaS}_2$ show metallic behavior based on the $\rho_{xx}(T)$ curve [27,28], even though the concentration of intercalating Co atoms is close to the one in the present work. However, in these studies, the crystal structure of both $\text{Co}_{0.26}\text{TaS}_2$ and $\text{Co}_{0.29}\text{TaS}_2$ was refined with space group $P6_322$, which means the Co atoms were in the form of $\sqrt{3} \times \sqrt{3}$ superstructures.

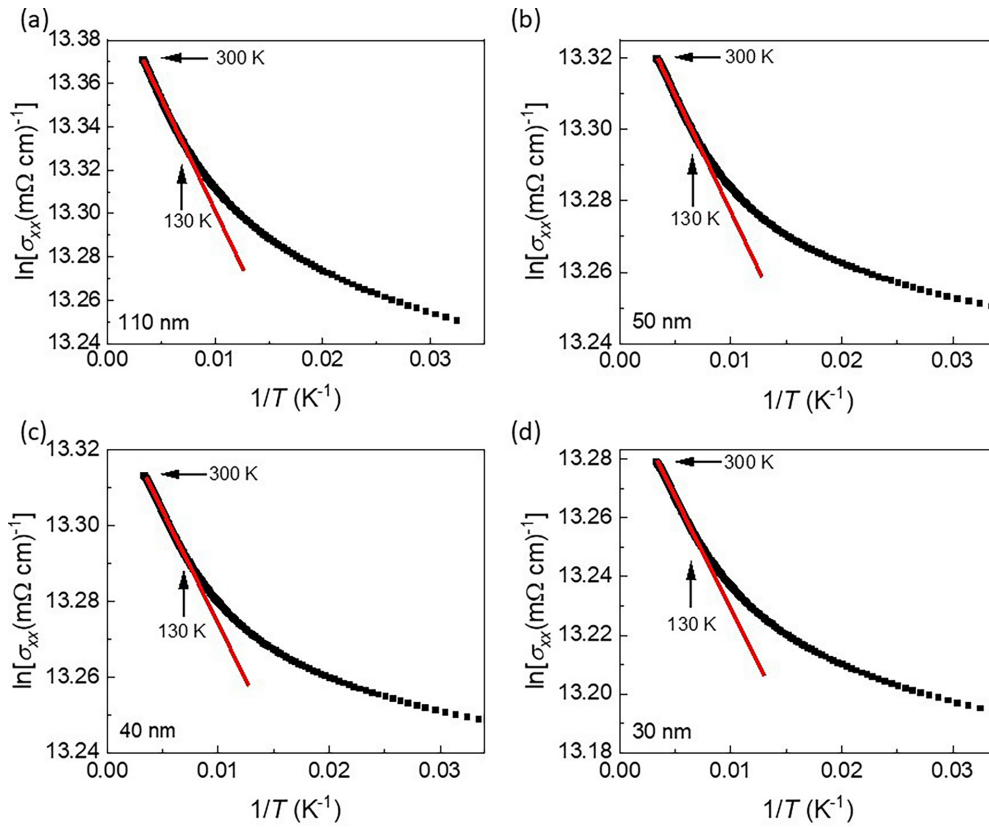


FIG. 4. High-temperature ($T > 130$ K) electronic transport can be fitted using the nearest-neighbor hopping model. The red solid lines serve as a visual guide.

Therefore, the type of intercalation (i.e., ordered or disordered) should have a strong effect on the transport properties of Co_xTaS_2 . In addition, the charge carriers in disordered systems are expected to hop between sites with a variable hopping distance, which is consistent with the low-temperature electronic transport properties of $\text{Co}_{0.27}\text{TaS}_2$ shown below.

To better understand the charge transport mechanism, we plotted the logarithmic conductivity as a function of temperature. In the high-temperature range (130–300 K), the charge transport can be described using the nearest neighbor hopping (NNH) model for the disordered materials, where the electrons can only hop to the nearest neighbor site [29]. The NNH can be expressed as $\sigma = \sigma_0 \exp(-E_a/K_B T)$, where σ_0 is the pre-exponential factor, E_a denotes the activation energy, and K_B is the Boltzmann constant [30,31]. All curves for devices with different thicknesses show a linear dependence, $\ln \sigma$ vs $1/T$ for $T > 130$ K; see Figs. 4(a)–4(d). We then determined the activation energy that governs the hopping of the carriers to be 0.5–0.9 meV, which is much smaller than the thermal agitation at the measuring temperature range 130–300 K (corresponding to 11–26 meV), indicating that the conduction mechanism is dominated by the thermal activation and leads to exponential temperature dependence, $\sigma = \sigma_0 \exp(-E_a/K_B T)$ [30].

At low temperatures, when the thermal energy becomes insufficient, hopping is governed by the energy of the available sites. Therefore, the electron continues hopping to a site where the potential difference is smaller [32]. This transition

can be expressed by the variable-range hopping (VRH) model, where the conductivity is given as $\sigma = \sigma_0 \exp(T/T_0)^{1/(n+1)}$, with $n = 1, 2, \text{ or } 3$ for 1D, 2D, or 3D, depending on the VRH mechanism [30–32]. The VRH mechanism was investigated for devices with different thicknesses. At $T < 130$ K, the logarithmic conductivity, $\ln(\sigma_{xx})$ vs $T^{1/4}$ of the 110-nm device, shows the best linearity; see Fig. 5(a). In contrast, $\ln(\sigma_{xx})$ as a function of $T^{1/3}$ [Figs. 5(b)–5(d)] shows higher linearity for the 30-, 40-, and 50-nm-thick devices of the same temperature range. The dominant conduction mechanism in the devices changed from the 3D- to the 2D-VRH mechanism as the thickness decreased from 110 to 50 nm. This may be because the disorder reduced with decreasing thickness, and the conduction mechanism modified where the mean free path becomes larger. An alternative explanation is that the thickness of the devices becomes comparable to the size of the localized states' wave function [33].

To better understand the electronic transport properties for the nanoflake devices (30–110 nm), we measured the isothermal Hall resistivity (ρ_{xy}) as a function of a perpendicular magnetic field for a 50-nm-thick device at $T = 2$ K; see Fig. 6(a). The hysteresis loop indicates that the $\text{Co}_{0.27}\text{TaS}_2$ flake has an out-of-plane magnetic anisotropy, even when the thickness of the flake decreased to 50 nm. Compared to the $M(H)$ hysteresis loop of the bulk crystal in Fig. 2(e), we found that the remnant to saturation magnetization ratio $M_r/M_s = 0.74$ (or $\rho_{xy(r)}/\rho_{xy(s)} = 0.69$) decreased to $\rho_{xy(r)}/\rho_{xy(s)} = 0.55$ for the 50-nm-thick devices, and the coercive field becomes

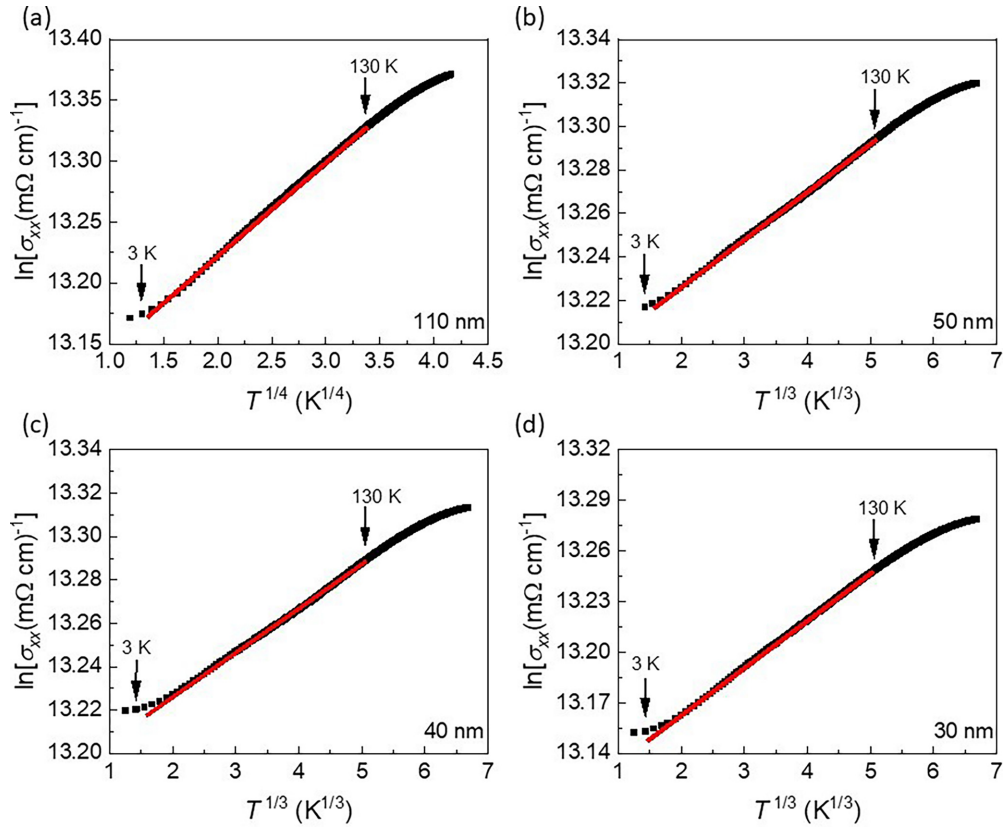


FIG. 5. Conductivity at low temperatures ($T < 130$ K) fitted using the variable-range hopping VRH model. (a) Conductivity is governed by the 3D VRH mechanism. (b)–(d) Conductivity is governed by the 2D VRH mechanism. The red solid lines are guides for the eye.

smaller with decreasing thickness (see Fig. 8). In the plot, we have eliminated the longitudinal contribution due to the misalignment of the Hall electrodes from the anomalous Hall resistance by using $\rho_{xy} = [\rho_{xy}(+H) - \rho_{xy}(-H)]/2$. At $T \approx 30$ K, the curve loses the hysteretic behavior, which indicates the T_C is around 30 K. As the temperature increases further, the AHE disappears gradually, and the curve becomes more linear as the material becomes more paramagnetic; see Fig. 6(b). The Hall resistivity of ferromagnetic materials is commonly expressed as $\rho_{xy} = R_o H + \rho_{xy}^{AH}$, where R_o and ρ_{xy}^{AH} denote the ordinary Hall coefficient and anomalous resistivity, respectively. As can be seen in Figs. 2(e) and 6(b), both magnetization and Hall resistivity do not saturate in a high field, hence, a linear fit cannot be used here. Alternatively, the Hall resistivity at the highest field (90 kOe in this study) can be used as an approximation of the anomalous Hall resistivity ρ_{xy}^{AH} because the ordinary Hall resistivity is negligible compared to the anomalous Hall resistivity. Furthermore, the AHE can be attributed either to the intrinsic effect related to the Berry curvature or the extrinsic contributions that arise from a side-jump or skew scattering [34,35]. The intrinsic contribution of the anomalous Hall conductivity σ_{xy}^{AH} can be estimated using e^2/hd , where e is the electronic charge, h denotes the Plank constant, and d is the lattice parameter [36,37]. To compare the theoretically predicted value ($\sim 802 \Omega^{-1} \text{ cm}^{-1}$) with the experimental data, the temperature dependence of the anomalous Hall conductivity $\sigma_{xy}^{AH} \approx \frac{\rho_{xy}^{AH}}{\rho_{xx}^2}$ is shown in Fig. 6(c). At 2 K, σ_{xy}^{AH} is $20.65 \Omega^{-1} \text{ cm}^{-1}$, which is lower than the

theoretical value. This indicates that the AHE is not dominated by an intrinsic mechanism. The side-jump contribution can also be estimated, theoretically, using the $(e^2/hd)(\varepsilon_{so}/E_f)$, where ε_{so} is the spin-orbital interaction energy. For metallic ferromagnets, ε_{so}/E_f generally ranges 0.001–0.01 and the higher limit is commonly used to estimate the side-jump contribution [37,38].

Usually, both skew-scattering and the side-jump mechanism obey the scaling relation $\rho_{xy}^{AH} = \beta \rho_{xx}^\alpha$, with $\alpha = 1$ for skew scattering and $\alpha = 2$ for intrinsic and side-jump contributions. Recently, a following modified scaling law has been proposed [39,40]:

$$\begin{aligned} \rho_{xy}^{AH} &= \alpha \rho_{xx0} + \beta_0 \rho_{xx0}^2 + \gamma \rho_{xx0} \rho_{xxT} + \beta_1 \rho_{xxT}^2 \\ &= C + a \rho_{xxT} + \beta_1 \rho_{xxT}^2. \end{aligned}$$

Here, α is the skew-scattering coefficient, the coefficients β_0 , β_1 , and γ contain intrinsic Berry curvature and side-jump contributions, ρ_{xx0} is the residual resistivity, $\rho_{xxT} = \rho_{xx} - \rho_{xx0}$, $C = \alpha \rho_{xx0} + \beta_0 \rho_{xx0}^2$, and $a = \gamma \rho_{xx0}$. As can be seen in Fig. 6(d), the linear behavior of the anomalous resistivity ρ_{xy}^{AH} and the ρ_{xxT}^2 plot suggests that the side-jump mechanism should be the dominating contribution to the AHE in this material. Note that not only the side-jump but also the intrinsic mechanism is proportional to ρ_{xx}^2 [34]. In other words, we cannot exclude an intrinsic contribution. However, based on the presented data, we can conclude that the side jump is the main contributor to the AHE. This is justifiable because the randomly distributed Co atoms and Co vacancies can be

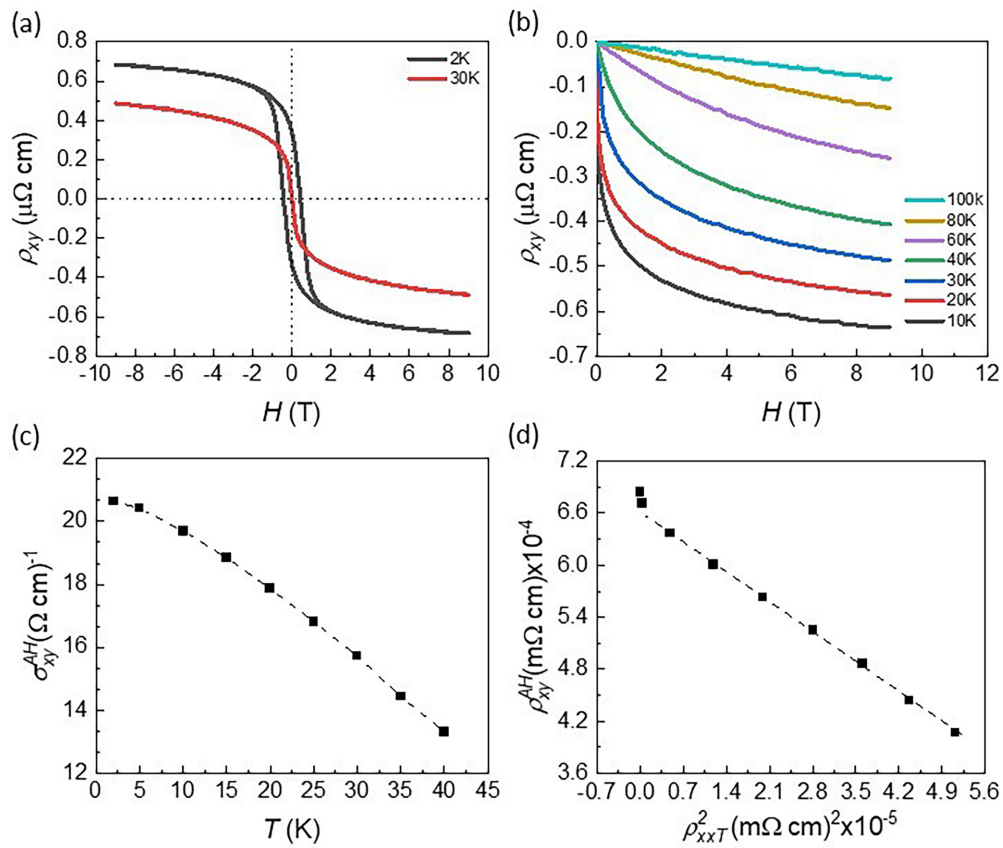


FIG. 6. Electronic properties of a 50-nm-thick device. Hall resistivities at (a) 2 K and (b) 10–100 K. (c) Temperature dependence of the anomalous Hall conductivity σ_{xy}^{AH} at 90 KOe. (d) ρ_{xy}^{AH} plotted against ρ_{xxT}^2 . The dashed lines serve as a guide for the eyes.

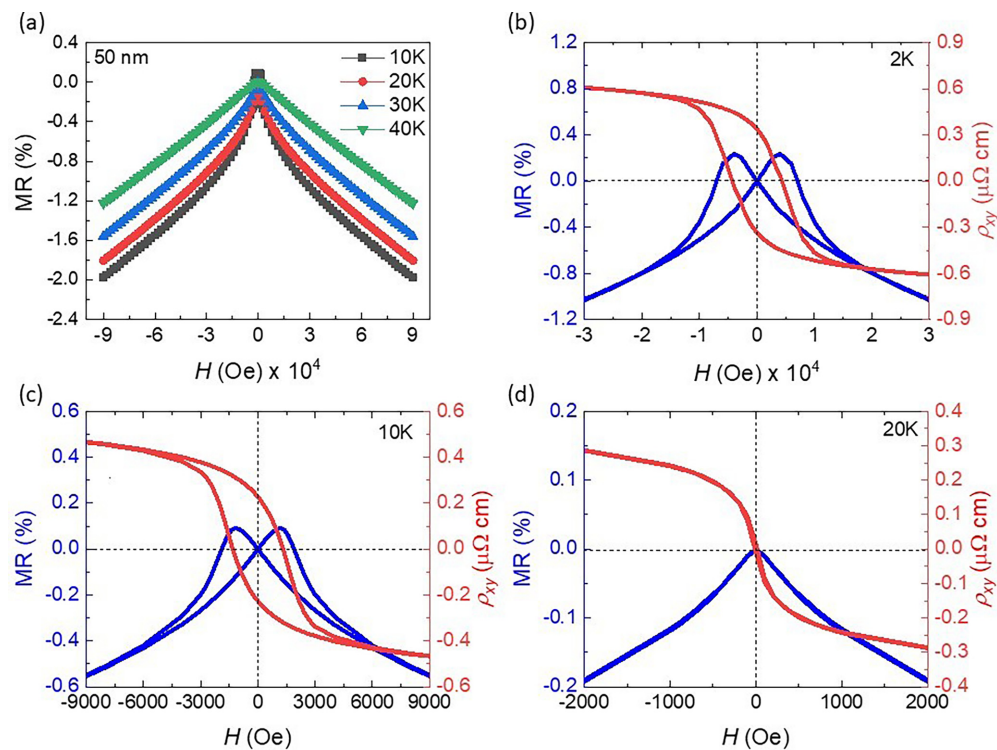


FIG. 7. Magnetoresistance MR measurements of 50-nm device (a) at 10–40 K. (b)–(d) Field dependent of MR and ρ_{xy} at 2, 10, and 20 K.

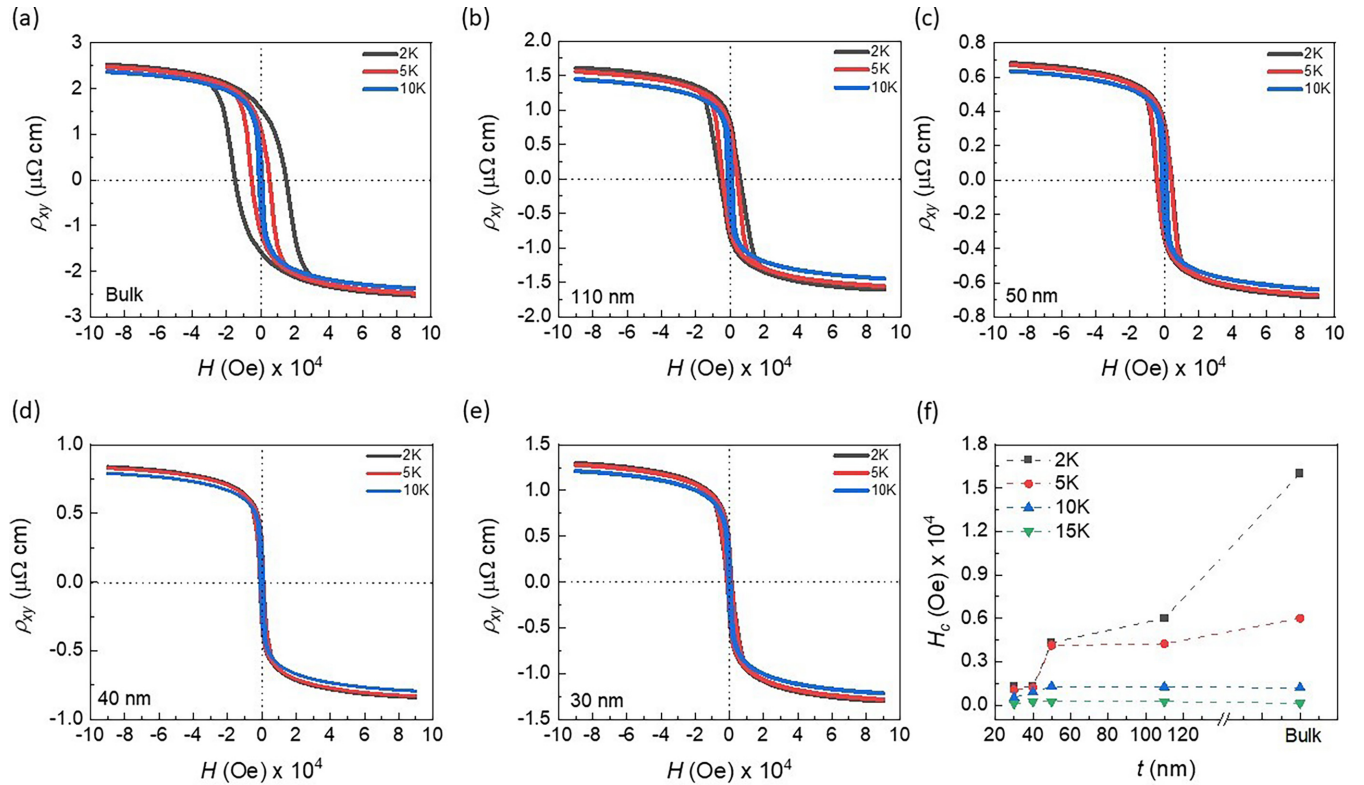


FIG. 8. (a)–(e) Measured anomalous Hall resistivity (ρ_{xy}) as a function of the applied field for bulk, 110-, 50-, 40-, 30-nm devices, at 2, 5, and 10 K. (f) H_c vs T for devices with different thicknesses.

regarded as impurities and defects, which are responsible for the dominant extrinsic scattering mechanism to the AHE.

Magnetoresistance (MR) was also examined by sweeping the magnetic field along the c axis from 90 to -90 kOe at selected temperatures. Usually, in disordered or doped low-dimensional systems a negative MR is observed [30]. The disorder affects the electronic properties substantially and alters the MR from positive to negative. This was reported for mechanically exfoliated monolayer graphene [41]. As shown in Fig. 7(a), the MR of the 50-nm sample is negative at all temperatures, which is expected for a disordered system. The MR is defined as $[R(H) - R(0)/R(0)] \times 100\%$, where $R(H)$ and $R(0)$ denote the resistance for a field H and zero field, respectively. Sweeping the field at low temperatures resulted in a bowtie-shaped curve, where the MR reached the maximum at H_c and then decreased with increasing magnetic field strength. Subsequently, the same behavior was observed for the negative field region; see Fig. 7(b). A non-saturated MR of about 2% was observed, and H_c at 2 K was estimated to be around 4000 Oe. As the temperature was increased, the bowtie shape disappeared, and both MR and H_c decreased. In addition, similar results were found for the Hall effect measurements where ρ_{xy} and H_c also decreased with increasing temperature. Very similar coercive fields in MR and ρ_{xy} were observed in the magnetotransport measurements of the samples. Figures 7(b)–7(d) show the MR and anomalous Hall resistivity of the 50-nm sample at 2, 10, and 20 K.

In addition, the thickness dependence of the transport properties of the materials can be studied using the anomalous

Hall resistivity versus the magnetic field, measured at 2 K. Shown in Fig. 8 are the hysteresis loops for samples ranging from bulk to nanoflake (30 nm). It appears that H_c depends strongly on the sample thickness; see Fig. 8(f). A similar outcome was reported for the van der Waals ferromagnetic $\text{Fe}_{0.29}\text{TaS}_2$, which was attributed to the thickness-dependent ferromagnetic domain structure [42]. Also, recently it was reported that the domain structure changes from labyrinth patterns (bulk limit) to fragmented domains (thinner flakes) of Fe_5GeTe_2 . This transition was attributed to the reduction of PMA as the thickness decreased [43]. The reason behind the H_c thickness dependence in $\text{Co}_{0.27}\text{TaS}_2$ might be that the domain structure changes with decreasing thickness. Further research may clarify this in the future.

IV. CONCLUSION

In summary, we reported the disordered intercalation of magnetic ions (Co) between the vdW gaps of $2H$ - TaS_2 . This was confirmed by the SC-XRD refinement and the absence of $(1/2 \ 1/2 \ 0)$ or $(1/3 \ 1/3 \ 0)$ diffraction spots in the SAED patterns. The obtained $\text{Co}_{0.27}\text{TaS}_2$ shows perpendicular magnetic anisotropy, and it can be exfoliated easily down to nanoflakes. As a result of the disordered intercalation, the temperature-dependent conductivity of $\text{Co}_{0.27}\text{TaS}_2$ exhibits semiconductorlike behavior. This can be attributed to the hopping of electrons across the temperature range 2–300 K. Specifically, it was found that nearest-neighbor hopping of electrons is the dominating conduction mechanism at high temperatures, whereas variable-range hopping prevails

at low temperatures (because the thermal energy is too low to facilitate nearest-neighbor hopping). In addition, the magnetotransport properties of $\text{Co}_{0.27}\text{TaS}_2$ with different thicknesses were investigated. The obtained anomalous Hall resistivity data show that the dominant AHE mechanism is the extrinsic side jump.

ACKNOWLEDGMENT

This work was supported by King Abdullah University of Science and Technology (KAUST) Office of Sponsored Research (OSR) under Awards No. ORA-CRG8-2019-4081 and No. ORA-CRG10-2021-4665.

- [1] Z. Wang, R. Li, C. Su, and K. P. Loh, Intercalated phases of transition metal dichalcogenides, *SmartMat* **1**, e1013 (2020).
- [2] S. Husain, R. Gupta, A. Kumar, P. Kumar, N. Behera, R. Brucas, S. Chaudhary, and P. Svedlindh, Emergence of spin-orbit torques in 2D transition metal dichalcogenides: A status update, *Appl. Phys. Rev.* **7**, 041312 (2020).
- [3] M. Chhowalla, H. S. Shin, G. Eda, L.-J. Li, K. P. Loh, and H. Zhang, The chemistry of two-dimensional layered transition metal dichalcogenide nanosheets, *Nat. Chem.* **5**, 263 (2013).
- [4] A. K. Geim and I. V. Grigorieva, Van der Waals heterostructures, *Nature (London)* **499**, 419 (2013).
- [5] Y. Zhang, Y.-W. Tan, H. L. Stormer, and P. Kim, Experimental observation of the quantum Hall effect and Berry's phase in graphene, *Nature (London)* **438**, 201 (2005).
- [6] C. Gong, L. Li, Z. Li, H. Ji, A. Stern, Y. Xia, T. Cao, W. Bao, C. Wang, and Y. Wang, Discovery of intrinsic ferromagnetism in two-dimensional van der Waals crystals, *Nature (London)* **546**, 265 (2017).
- [7] B. Huang, G. Clark, E. Navarro-Moratalla, D. R. Klein, R. Cheng, K. L. Seyler, D. Zhong, E. Schmidgall, M. A. McGuire, and D. H. Cobden, Layer-dependent ferromagnetism in a van der Waals crystal down to the monolayer limit, *Nature (London)* **546**, 270 (2017).
- [8] W. Xing, Y. Chen, P. M. Odenthal, X. Zhang, W. Yuan, T. Su, Q. Song, T. Wang, J. Zhong, and S. Jia, Electric field effect in multilayer $\text{Cr}_2\text{Ge}_2\text{Te}_6$: A ferromagnetic 2D material, *2D Mater.* **4**, 024009 (2017).
- [9] Y. Wang, C. Xian, J. Wang, B. Liu, L. Ling, L. Zhang, L. Cao, Z. Qu, and Y. Xiong, Anisotropic anomalous Hall effect in triangular itinerant ferromagnet Fe_3GeTe_2 , *Phys. Rev. B* **96**, 134428 (2017).
- [10] M. Rajapakse, B. Karki, U. O. Abu, S. Pishgar, M. R. K. Musa, S. Riyadh, M. Yu, G. Sumanasekera, and J. B. Jasinski, Intercalation as a versatile tool for fabrication, property tuning, and phase transitions in 2D materials, *npj 2D Mater. Appl.* **5**, 30 (2021).
- [11] S. Parkin and R. Friend, 3 d transition-metal intercalates of the niobium and tantalum dichalcogenides. I. Magnetic properties, *Philos. Mag. B* **41**, 65 (1980).
- [12] M. Inoue, H. Hughes, and A. Yoffe, The electronic and magnetic properties of the 3d transition metal intercalates of TiS_2 , *Adv. Phys.* **38**, 565 (1989).
- [13] R. Friend, A. Beal, and A. Yoffe, Electrical and magnetic properties of some first row transition metal intercalates of niobium disulphide, *Philos. Mag.: J. Theor. Exp. Appl. Phys.* **35**, 1269 (1977).
- [14] B. Van Laar, H. Rietveld, and D. Ijdo, Magnetic and crystallographic structures of Me_xNbS_2 and Me_xTaS_2 , *J. Solid State Chem.* **3**, 154 (1971).
- [15] M. Eibschütz, S. Mahajan, F. DiSalvo, G. Hull, and J. Waszczak, Ferromagnetism in metallic intercalated compounds Fe_xTaS_2 ($0.20 \leq x \leq 0.34$), *J. Appl. Phys.* **52**, 2098 (1981).
- [16] C. Zhang, Y. Yuan, M. Wang, P. Li, J. Zhang, Y. Wen, S. Zhou, and X.-X. Zhang, Critical behavior of intercalated quasi-van der Waals ferromagnet $\text{Fe}_{0.26}\text{TaS}_2$, *Phys. Rev. Mater.* **3**, 114403 (2019).
- [17] C. Li, J. Wu, R. Bian, G. Cao, E. Pan, Z. Liu, J. Yu, H. Hosono, and F. Liu, 2D magnetic $\text{Fe}_{0.75}\text{Ta}_{0.5}\text{S}_2$: Giant exchange bias with broadband photoresponse, *Adv. Funct. Mater.* **32**, 2208531 (2022).
- [18] S. Husremovic, C. K. Groschner, K. Inzani, I. M. Craig, K. C. Bustillo, P. Ercius, N. P. Kazmierczak, J. Syndikus, M. Van Winkle, S. Aloni, T. Taniguchi, K. Watanabe, S. M. Griffin, and D. K. Bediako, Hard ferromagnetism down to the thinnest limit of iron-intercalated tantalum disulfide, *J. Am. Chem. Soc.* **144**, 12167 (2022).
- [19] S. Polesya, S. Mankovsky, H. Ebert, P. G. Naumov, M. A. ElGhazali, W. Schnelle, S. Medvedev, S. Mangelsen, and W. Bensch, $\text{Mn}_{1/4}\text{NbS}_2$: Magnetic and magnetotransport properties at ambient pressure and ferro- to antiferromagnetic transition under pressure, *Phys. Rev. B* **102**, 174423 (2020).
- [20] S. K. Karna, F. N. Womack, R. Chapai, D. P. Young, M. Marshall, W. Xie, D. Graf, Y. Wu, H. Cao, L. DeBeer-Schmitt, P. W. Adams, R. Jin, and J. F. DiTusa, Consequences of magnetic ordering in chiral $\text{Mn}_{1/3}\text{NbS}_2$, *Phys. Rev. B* **100**, 184413 (2019).
- [21] C. Zhang, J. Zhang, C. Liu, S. Zhang, Y. Yuan, P. Li, Y. Wen, Z. Jiang, B. Zhou, Y. Lei, D. Zheng, C. Song, Z. Hou, W. Mi, U. Schwingenschlogl, A. Manchon, Z. Q. Qiu, H. N. Alshareef, Y. Peng, and X. X. Zhang, Chiral helimagnetism and one-dimensional magnetic solitons in a cr-intercalated transition metal dichalcogenide, *Adv. Mater.* **33**, 2101131 (2021).
- [22] G. Sheldrick, Crystal structure refinement with SHELXL, *Acta Crystallogr. Sect. C: Struct. Chem.* **71**, 3 (2015).
- [23] C. Zhang, C. Liu, S. Zhang, B. Zhou, C. Guan, Y. Ma, H. Algaidi, D. Zheng, Y. Li, and X. He, Magnetic skyrmions with unconventional helicity polarization in a van der Waals ferromagnet, *Adv. Mater.* **34**, 2204163 (2022).
- [24] See Supplemental Materials at <http://link.aps.org/supplemental/10.1103/PhysRevB.107.134406> for the EDX and XRD results.
- [25] Y. Horibe, J. Yang, Y.-H. Cho, X. Luo, S. B. Kim, Y. S. Oh, F.-T. Huang, T. Asada, M. Tanimura, and D. Jeong, Color theorems, chiral domain topology, and magnetic properties of Fe_xTaS_2 , *J. Am. Chem. Soc.* **136**, 8368 (2014).
- [26] P. Park, Y.-G. Kang, J. Kim, K. H. Lee, H.-J. Noh, M. J. Han, and J.-G. Park, Field-tunable toroidal moment and anomalous Hall effect in noncollinear antiferromagnetic Weyl semimetal $\text{Co}_{1/3}\text{TaS}_2$, *npj Quantum Mater.* **7**, 42 (2022).

- [27] H. Wang, J.-F. Lin, X.-Y. Zeng, X.-P. Ma, J. Gong, Z.-Y. Dai, X.-Y. Wang, K. Han, Y.-T. Wang, and T.-L. Xia, Large anomalous Hall effect in layered antiferromagnet $\text{Co}_{0.29}\text{TaS}_2$, [arXiv:2203.12771](#).
- [28] Y. Liu, Z. Hu, X. Tong, E. D. Bauer, and C. Petrovic, Electrical and thermal transport in van der Waals magnets $2\text{H-M}_x\text{TaS}_2$ ($M = \text{Mn, Co}$), [Phys. Rev. Res.](#) **4**, 013048 (2022).
- [29] V. F. Gantmakher, *Electrons and Disorder in Solids* (Oxford University Press, Oxford, 2005), Vol. 130.
- [30] W. Bai, Z. Hu, S. Wang, Y. Hua, Z. Sun, C. Xiao, and Y. Xie, Intrinsic negative magnetoresistance in van der Waals FeNbTe_2 single crystals, [Adv. Mater.](#) **31**, 1900246 (2019).
- [31] M. Rudra, H. Tripathi, A. Dutta, and T. Sinha, Existence of nearest-neighbor and variable range hopping in $\text{Pr}_2\text{ZnMnO}_6$ oxygen-intercalated pseudocapacitor electrode, [Mater. Chem. Phys.](#) **258**, 123907 (2021).
- [32] J. Bellissard, Coherent and dissipative transport in aperiodic solids: An overview, *Dynamics of Dissipation*, edited by P. Garbaczewski and R. Olkiewicz, Lecture Notes in Physics, Vol. 597 (Springer, Berlin, Heidelberg, 2002), pp. 413–485.
- [33] H. Liu, H. S. Choe, Y. Chen, J. Suh, C. Ko, S. Tongay, and J. Wu, Variable range hopping electric and thermoelectric transport in anisotropic black phosphorus, [Appl. Phys. Lett.](#) **111**, 102101 (2017).
- [34] N. Nagaosa, J. Sinova, S. Onoda, A. H. MacDonald, and N. P. Ong, Anomalous hall effect, [Rev. Mod. Phys.](#) **82**, 1539 (2010).
- [35] S. Onoda, N. Sugimoto, and N. Nagaosa, Quantum transport theory of anomalous electric, thermoelectric, and thermal Hall effects in ferromagnets, [Phys. Rev. B](#) **77**, 165103 (2008).
- [36] P. Nozieres and C. Lewiner, A simple theory of the anomalous Hall effect in semiconductors, [J. Phys.](#) **34**, 901 (1973).
- [37] S. Onoda, N. Sugimoto, and N. Nagaosa, Intrinsic Versus Extrinsic Anomalous Hall Effect in Ferromagnets, [Phys. Rev. Lett.](#) **97**, 126602 (2006).
- [38] Q. Wang, Y. Xu, R. Lou, Z. Liu, M. Li, Y. Huang, D. Shen, H. Weng, S. Wang, and H. Lei, Large intrinsic anomalous Hall effect in half-metallic ferromagnet $\text{Co}_3\text{Sn}_2\text{S}_2$ with magnetic Weyl fermions, [Nat. Commun.](#) **9**, 3681 (2018).
- [39] D. Hou, G. Su, Y. Tian, X. Jin, S. A. Yang, and Q. Niu, Multi-variable Scaling for the Anomalous Hall Effect, [Phys. Rev. Lett.](#) **114**, 217203 (2015).
- [40] B. Lv, P. Liu, Y. Wang, C. Gao, and M. Si, A large anomalous Hall conductivity induced by Weyl nodal lines in $\text{Fe}_{70}\text{Al}_{30}$, [Appl. Phys. Lett.](#) **121**, 072405 (2022).
- [41] Y.-B. Zhou, B.-H. Han, Z.-M. Liao, H.-C. Wu, and D.-P. Yu, From positive to negative magnetoresistance in graphene with increasing disorder, [Appl. Phys. Lett.](#) **98**, 222502 (2011).
- [42] R. Cai, W. Xing, H. Zhou, B. Li, Y. Chen, Y. Yao, Y. Ma, X. C. Xie, S. Jia, and W. Han, Anomalous Hall effect mechanisms in the quasi-two-dimensional van der Waals ferromagnet $\text{Fe}_{0.29}\text{TaS}_2$, [Phys. Rev. B](#) **100**, 054430 (2019).
- [43] R. Fujita, P. Bassirian, Z. Li, Y. Guo, M. A. Mawass, F. Kronast, G. van der Laan, and T. Hesjedal, Layer-dependent magnetic domains in atomically thin Fe_3GeTe_2 , [ACS Nano](#) **16**, 10545 (2022).